LAWRENCE
LIVERMORE
NATIONAL
LABORATORY

LLNL-JRNL-859011

Microstructural evolution of rapidly solidified hypoeutectic Al-10Cu alloy during non-isothermal annealing transients induced by nano-second laser pulses

B. Vishwanadh, J. T. McKeown, J. Wiezorek

January 10, 2024

Materials Characterization

Disclaimer

LLNL-JRNL-859011

Microstructural evolution of rapidly solidified hypoeutectic Al-10Cu alloy during non-isothermal annealing transients induced by nano-second laser pulses

B. Vishwanadh,[1,*] J.T. McKeown,[2] J.M.K. Wiezorek[1,**]

[1] Department of Mechanical Engineering and Materials Science, Swanson School of Engineering, 636 Benedum Hall, 3700 O'Hara Street, Pittsburgh, PA 15261, USA

[2] Materials Science Division, Physical and Life Sciences Directorate, Lawrence Livermore National Laboratory, 7000 East Avenue, Livermore, CA 94551, USA

Abstract

The evolution of characteristic nonequilibrium features presenting in morphologically distinct regions of rapid solidification (RS) microstructures in a hypoeutectic Al-10Cu (atomic %) in response to non-isothermal annealing transients has been studied by transmission electron microscopy (TEM). The capabilities of the Movie-Mode Dynamic TEM (MM-DTEM) instrument were used to expose select regions of the RS microstructure to sequences of rapid heating and cooling transients induced by nanosecond laser pulses while permitting in-situ observation. Partial melting, microstructural scale coarsening, morphological changes of the nonequilibrium features in the multi-phase RS microstructure, and solid-state phase transformation were observed. Heterogeneous nucleation of nanoscale q-Al_2Cu phase involved metastable supersaturated α-Al and the θ'-Al_2Cu phases, establishing different sets of orientation relationships for the stable θ-Al_2Cu and α-Al phases. Replacement of banded morphology grains that formed under conditions driven farthest from equilibrium by an equiaxed nanocrystalline structure comprised of α-Al phase, the primary solidification product, and an intergranular network of Al_2Cu crystals has been attributed to local remelting. The experimental approach explored here permitted discovery of mechanistic details of location-specific transformation pathways activated in the multi-phase RS microstructure of hypoeutectic Al-Cu during subsequent nonisothermal transients.

[*]Now at Materials Science Division, Bhabha Atomic Research Centre, Mumbai, India

[**]Corresponding author, wiezorek@pitt.edu

1. Introduction

Fusion-based additive manufacturing (AM) technologies, such as selective laser melting (SLM) of powder feedstock in laser powder-bed fusion (LPBF) and direct energy deposition (DED) of powder or wire feedstocks, utilize digitized designs to build a component by depositing the respective material in controlled patterns using layer-upon-layer processes on top of a solid substrate [1–3]. In metal SLM AM, a laser as a transient heat source melts relatively small volumes of feedstock material which fuse to the surrounding solid upon re-solidification with cooling rates in the range of $\approx 10^3$ K/s (e.g., DED) to $\approx 10^7$ K/s (e.g., LPBF) [4–6]. The initial thermal transient in the material of a given layer deposited in SLM AM produces rapid solidification (RS) microstructures by directional crystal growth behind accelerating solidification interfaces migrating at maximum rates, v, ranging from ≈ mm/s (e.g., DED) to m/s (LPBF) [6,7]. RS microstructures exhibit nonequilibrium features that depend on alloy composition, thermal gradient, and solidification rate [8]. These features can include scale refinements, solute trapping, modified solute segregation patterns, and formation of unexpected and metastable phases, including non-crystalline structures [8]. The layer-upon-layer build processes in SLM AM expose the RS microstructures developed in the initial thermal transient to additional transients of rapid heating and cooling during subsequent laser scan passes and deposition of subsequent layers. For example, the second thermal transients typically result in partial re-melting and/or non-isothermal annealing of the RS microstructures. The nonequilibrium features of the RS microstructures evolve during exposures to the subsequent non-isothermal transients. The number of thermal cycles and details of the specific heating and cooling rates can vary for different locations of the component fabricated by SLM AM, and heterogeneous microstructures and residual stresses develop [9–13]. The microstructures of SLM AM-derived parts are therefore produced by multiple non-isothermal annealing cycles of RS microstructures.

As summarized in several recent reviews of metal SLM AM, a host of post-mortem studies have revealed effects of changes in process parameters on details of the resulting microstructure for various alloys(e.g., Al-, Ni-, Ti-alloys and steels), generally confirming development of heterogeneity and reporting the presence of alloy and process-specific nonequilibrium features [9–13]. However, mechanistic details of the sequences of the relevant transitions evolving the RS microstructures in response to the individual rapid non-isothermal transients intrinsic to SLM AM have not been elucidated and warrant additional study. Thermodynamic considerations imply that

microstructural changes of the nonequilibrium RS microstructures during annealing will include grain and secondary-phase coarsening, composition homogenization, solid-solid phase transformations of metastable phases to thermodynamically more stable phases, and dislocation sub-structure modifications resulting from thermomechanical stress cycling. Unlike in isothermal annealing heat treatments, thermal and thermo-mechanical driving forces and atomic mobilities change rapidly during laser heating–induced non-isothermal transients associated with SLM AM. These transients are of short durations, typically on the order of 10^{-5} s to 10^{-2} s [9–13]. Furthermore, the altered nonequilibrium solute segregation patterns, intragranular dislocation structures, and often severe scale refinements observed in RS microstructures of multi-phase alloys would be expected to influence nucleation and growth behaviors during annealing, consequently affecting the resulting properties. Hence, mechanistic details of the pathways selected for the respective transformations during evolution of the nonequilibrium RS microstructure in response to the sequential exposures to non-isothermal transients may differ from those established for isothermal annealing treatments. This is evident from the need for modified post-build heat treatments of SLM-AM parts when compared with heat treatment schema established for conventionally manufactured product [14–17].

Since reliable structural and thermophysical data are readily available for phases presenting in the Al-Cu system for the composition range of Al to Al_2Cu (i.e., the eutectic phase diagram section with terminal phases of α-Al(Cu) solid solution and θ-Al_2Cu ordered intermetallic), it has served frequently as a model system in basic research on solid-solid and liquid-solid phase transformations in dilute (Cu < 2.5 atomic percent, at.%) and concentrated multicomponent alloys (≈ 3 at.% ≤ Cu < ≈ 32 at.%) [18–21]. Many fundamental aspects of our understanding of solid-state transformations (e.g., precipitate formation and dissolution) and for solidification microstructure evolution have been elaborated via studies employing Al-Cu alloys [8, 21–23]. For example, post-mortem and in-situ heating TEM have been used to determine morphological and crystallographic aspects, interfacial structure, and growth kinetics of θ-Al_2Cu phase formation in the α–Al grains during isothermal annealing of dilute Al-Cu alloys, such as aging of precipitation strengthening Al-1.7at.%Cu (corresponding in weight percent, wt.%, to Al-4 wt.% Cu) [24–27]. Mechanisms for formation of θ-phase precipitates from the matrix of the α-phase lattice in dilute Al(Cu) alloys in the presence of metastable θ'-phase have been proposed, but confirmation by direct TEM observations is still lacking [18,21,28,29].

RS microstructure evolution after laser melting has been studied by in-situ transmission electron microscopy (TEM) and post-mortem characterization for hypoeutectic, eutectic, and hypereutectic Al-Cu alloys [30–37]. The multiphase RS microstructures developed in nanoscale thin films of Al-Cu alloys after laser melting in the TEM have been shown to exhibit morphologically distinct zones equivalent to those observed in bulk samples after scanned laser surface melting [30,33,38]. Direct observation of the RS interface migration after pulsed laser melting during in-situ TEM experiments performed by Movie-Mode Dynamic TEM (MM-DTEM) has permitted determination of the solidification interface velocity evolution and robust correlation with nonequilibrium conditions at the solidification interface and growth modes responsible for the genesis of the characteristic nonequilibrium features of the multi-phase RS microstructures [30,33,38,39]. Results from these unique experiments have enabled quantitative comparisons with predictions of solidification theory regarding nonequilibrium solute trapping and validation of computer models for the simulation of RS microstructure evolution in Al-Cu alloys after laser melting [38,40–42].

In the current work we performed MM-DTEM experiments to study the evolution of the RS microstructure of hypoeutectic Al-10 at.% Cu alloy (Al-10Cu), corresponding to Al-21 wt.% Cu, during rapid non-isothermal transients induced by controlled sequences of pulsed laser irradiation. Effects of the laser pulse energy and the number of pulses applied subsequently to the initial transient that established the RS microstructure are reported. The transformation of nonequilibrium features of the distinct characteristic regions of the RS microstructure in response to non-isothermal heating-cooling transients imposed by additional laser irradiation annealing are discussed. The experimental results are suitable to support further development of mechanistically accurate computer models for simulation of alloy microstructure evolution during SLM AM and may assist emerging efforts exploring local in-situ tailoring of the as-built microstructures to achieve improved part performance [43–46].

2. Experimental Procedures and Materials

Nanocrystalline hypoeutectic Al-10Cu alloy thin films with thickness of ~ 100 nm were deposited on 50-nm-thick amorphous Si_3N_4 support membranes of square silicon window TEM grids. Dual electron beam evaporation (Pascal Technologies Dual E-Beam Deposition System) was performed with high-purity elemental Al and Cu targets in high vacuum ($< 5 \times 10^{-8}$ torr) condition

at a deposition rate of 2.0–2.5 nm/s with substrates held at 298 K. The thickness of the films was confirmed using a surface profilometer [47].

In-situ TEM RS and non-isothermal annealing experiments were performed in Movie-Mode operation with the DTEM (MM-DTEM) operating at 200 kV [25]. Single and multiple laser irradiation pulses of 15 ns duration from the sample drive laser of the MM-DTEM, a Nd:YAG laser operating in the near-infrared, with different energies ranging from nominally 0.4–1.1 μJ were used to induce locally rapid thermal transients that resulted in melting followed by solidification and/or non-isothermal annealing responses in the alloy thin films. The laser beam had a Gaussian profile ($1/e^2$ diameter of 135 ± 5 μm) and was incident at a 45º angle to the sample. This resulted in an elliptical shape for the laser pulse irradiated areas. Additional details of MM-DTEM in-situ RS experimentation have been described in detail previously [48]. RS microstructures were established by pulsed laser irradiation, the initial thermal transient, in up to five separate locations in the electron transparent window of the TEM grid specimen. The locations of the laser- induced melt pools were chosen to lie at safe distances, i.e., > ≈100 μm, away from the silicon support frame to avoid artifacts resulting from modifications of the radially symmetric directional heat extraction by the massive heat sink of the silicon frame [48]. By varying the laser pulse energy, an upper and lower bound for creation of RS microstructures were determined as ≈ 1.0 μJ and ≈ 0.7 μJ, respectively. For laser pulse energies larger than 1.0 μJ unacceptable levels of dewetting were observed, while for energy of ≈ 0.6 μJ melt pool formation was not readily discernible for the as-deposited state of the thin film specimens. The radial dimensions of the melt pools induced by the laser irradiation pulses, with nominal energy in the vicinity of ≈ 0.9 μJ, corresponded to ≈ 40% of the radial dimensions of the laser beam irradiated area on the thin film specimens. Changes in the laser pulse energy do not affect the dimensions of the irradiated area but influence the size of the melted areas and the details of the temporal behavior during re-solidification and creation of the RS microstructures. The RS microstructures established in the electron transparent window were exposed to additional laser pulses of 15 ns duration at selectively reduced energy relative to the energies of the respective melting pulse of the initial transient. This resulted in non-isothermal annealing or partial melting of the RS microstructures during these subsequent rapid and non-isothermal heating-cooling transients.

Post-mortem microstructural characterization was performed by scanning TEM (STEM) and TEM imaging and diffraction using a Tecnai G2 F20 UT (FEI/ThermoFisher) and a JEOL

JEM 2100F (JEOL Inc.) operated at 200 kV. Precession electron diffraction assisted automated crystal orientation mapping (PED-ACOM) was performed using an Astar/Topspin system (NanoMegas) attached to the Tecnai G2 F20 UT TEM for orientation imaging microscopy and crystallographic analysis of the annealed RS microstructures [49]. The PED-ACOM data was acquired with an electron probe of nominally 10 nm diameter for a precession half-angle of 0.75º and a step size of 10 nm. The maps of PED patterns were indexed with an angular resolution of 1˚ by computer-assisted matching with reciprocal space templates created for α-Al, θ-Al_2Cu, and θ'-Al_2Cu. For additional post-acquisition processing, analyses, and for visualization of the PED-ACOM data, commercial EBSD-OIM software (Apex, TSL, EDAX-Ametek) was used.

3. Results and Discussion

3.1 The as-deposited alloy microstructure

Fig.1(a) shows the microstructure of the as-deposited Al-Cu alloy, revealing the presence of equiaxial shape grains with an average size on the order of 50 nm diameter. The corresponding selected area electron diffraction (SAED) pattern is shown in Fig.1(b). The SAED pattern has been indexed with α-Al and θ-Al_2Cu phases only. Using TEM analysis by energy dispersive X-ray spectroscopy (EDXS) the average composition of the thin film has been determined as 9.6 (±0.5) at.% Cu and 90.4 (±0.5) at.% Al. The as-deposited Al-10Cu layers are comprised of nanocrystalline α-Al and θ-Al_2Cu grains, which is consistent with prior reports [30,33,37,38].

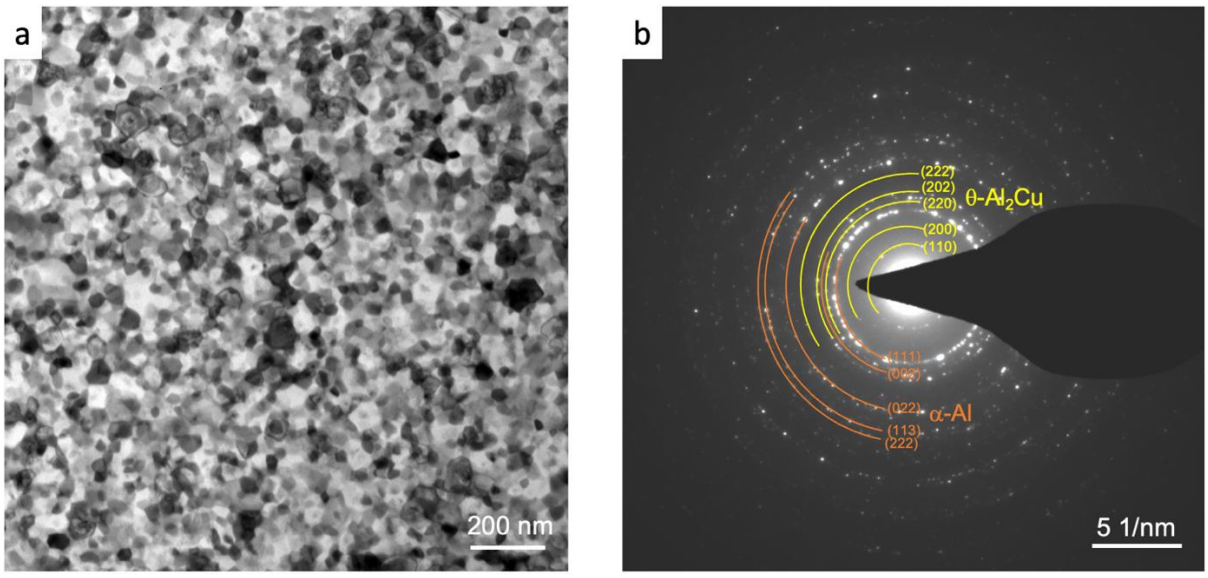

Fig. 1: a) Bright field (BF) TEM micrograph of the as-deposited Al-10Cu thin film and b) associated SAED pattern from a large field of view. Diffraction maxima associated with α-Al and θ-Al_2Cu phase are identified and marked and indexed in b) for convenience.

3.2 Microstructural response to sequences of non-isothermal annealing transients

Elliptically shaped regions of RS microstructure with dimensions of approximately 60-80 µm in diameter were created in the electron transparent window of the Al-10Cu TEM specimens in an initial thermal transient by pulsed laser irradiation with energy in the vicinity of 0.9 µJ using the MM-DTEM. The RS microstructures were then exposed to sequences of one, two, or three additional laser pulses of reduced energies relative to the first laser melting pulse with the goal to induce non-isothermal annealing responses. Examples of TEM images of the RS microstructures developed in five such experiments performed for the nanocrystalline Al-10Cu are shown as an overview and with higher spatial resolution as montages of representative sections in the TEM and STEM images of Fig. 2a and Fig. 3, respectively.

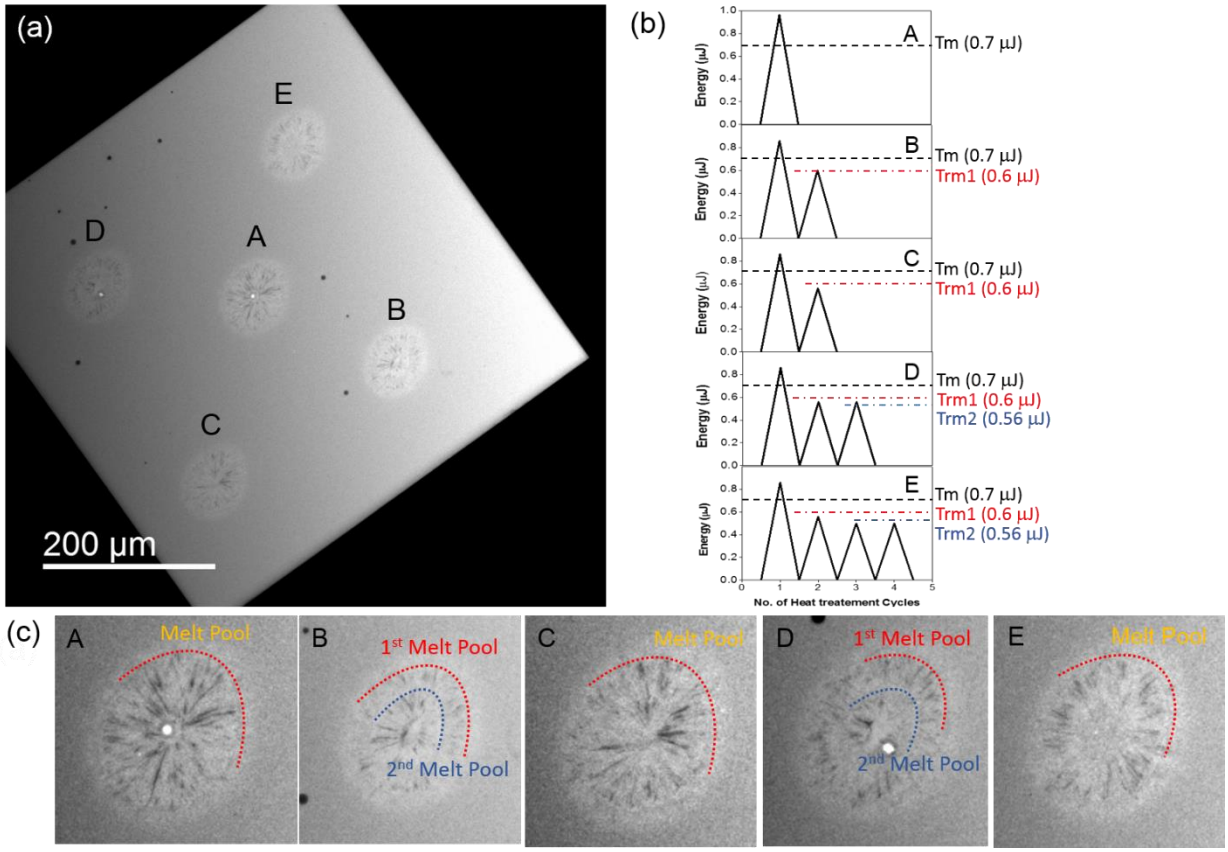

Fig. 2: a) Low-magnification overview TEM image of the square-shape electron transparent window with labels A to E marking separate pulsed-laser irradiated regions of the nanocrystalline Al-10Cu alloy. B) Schematics of the single, double, triple, and quadruple laser pulse irradiation schemes applied to locations marked A to E in a). The approximate laser energy threshold for melting of the original nanocrystalline alloy and the peak energy per pulse are marked according to experimental measurements by the dashed horizontal line and label Tm. The first pulse has sufficient energy to melt the as-deposited alloy and establishes RS microstructure for targeting by the subsequent laser irradiation pulses. Notably, in location B the second pulse had energy exceeding the threshold for melting of the RS microstructure (Trm1~0.6 µJ), and in location D the third pulse had energy exceeding the threshold of the non-isothermally annealed RS microstructure established after the second pulse of laser irradiation (Trm2~0.56 µJ). c) Higher magnification TEM images of the singly and multiply pulsed laser irradiated regions A to E in a). Marked by red dashed lines in c) panel B and in c) panel D are the perimeters of the original larger and a second smaller melt pools obtained after the first and the second laser pulse for location B in a), and the first and third laser pulse for location D in a), respectively.

The features near location marked A in Fig.2a represent the RS microstructure obtained after application of only a single laser pulse with an energy of 0.96 µJ, i.e., the result of the initial thermal transient of melting and re-solidification. The nanocrystalline microstructure of the as-

deposited state of the Al-10Cu gives the approximately uniform contrast in the square window of the Si TEM grid and the small dark spots are external contaminants (small dust/dirt particles). The RS microstructures at locations labeled B, C, D, and E in Fig. 2a have been exposed to a first laser pulse of sufficient energy, 0.86 μJ, to create a melt pool and then subsequently to one, two, and three additional laser pulses at reduced energies. The pulsed laser irradiation sequences applied to locations A to E in Fig. 2a are schematically depicted in Fig.2b as panels A to E. Magnified TEM images of the RS microstructures at locations A to E are shown as panel A to E in Fig.2c. For location A, the small bright contrast feature visible centrally in the RS microstructure represents a small hole that developed in the melt pool prior to re-solidification (Fig. 2a and Fig. 2c, panel A). This indicates localized dewetting of the alloy layer from the Si_3Ni_4 support film due to the high energy of the laser pulse resulting in a local hot spot. To avoid dewetting of the alloy layer, the laser energy was reduced to 0.86 μJ for the first irradiation pulse in subsequent experiments to develop the RS microstructures at locations marked as B to E in Fig. 2a.

The RS microstructure at location B in Fig. 2a was exposed to a second laser pulse of energy 0.6 μJ as indicated schematically in Fig. 2b, panel B. This resulted in formation of a second smaller melt pool in the central regions of the RS microstructure. The outer perimeters of the large first melt pool and of the smaller second melt pool are marked by dashed lines in Fig.2c, panel B for convenience. The formation of the second smaller melt pool in response to the second laser pulse implies that the threshold energy for melting differed for the as-deposited state and the RS microstructure of the Al-10Cu alloy film. The RS microstructure near label C in Fig. 2a was exposed to a second laser pulse of further reduced energy, 0.56 μJ, to avoid generation of a second melt pool. The resultant central region of the RS microstructure exhibits more prominent contrast features (Fig. 2c, panel C), which would be consistent with coarsening of the grain scale when compared with those observed by TEM bright-field (BF) imaging after single laser pulse irradiation (e.g., Fig. 2c, panel A). The RS microstructure established near the location labeled D in Fig. 2a was exposed to two additional lower energy, 0.56 μJ, irradiation pulses (Fig. 2b, panel D). Notably, the third laser pulse led to the formation of a smaller second melt pool in the central region of the larger area of RS microstructure established by the initial two thermal transients. The outer perimeters of the smaller and larger melt pools in the RS microstructure observed near location D in the Al-10Cu thin film are marked by dashed lines in Fig. 2c, panel D. To prevent melting of the RS microstructures during a third, fourth, and optional subsequent transients the

laser energy for third and fourth pulses, etc., were reduced to 0.5 μJ (Fig. 2c, panel E). The RS microstructure shown in Fig. 2a near location E and Fig. 2c, panel E, experienced a sequence of laser irradiation with four pulses, as depicted schematically in Fig. 2b, panel E. This RS microstructure is devoid of any dewetting or evidence for formation of a secondary melt pool. Postmortem analysis of the five RS microstructures shown in the overviews of Fig. 2 involved higher magnification STEM imaging and PED ACOM (Figs. 3, 4, 5 and 6).

3.2.1 Postmortem imaging of the non-isothermally annealed RS microstructures

Montages of BF STEM images of representative sections (left-to-right, perimeter-to-center of original melt pool established by first laser pulse) of the RS microstructures obtained at locations marked as A to E in Fig. 2a are shown in Fig. 3. The RS microstructure produced by the first laser pulse exhibited the four characteristic and morphologically distinct microstructural regions, marked as zones I, II, III, and IV in Fig. 3a, expected for hypoeutectic Al-Cu alloys [30,33,38]. Directional crystal growth started at the boundary between zone I and zone II and progressed towards the center of the melt pool established by the first laser pulse in the initial transient by formation of zone II, zone III, and then zone IV of the RS microstructures (directional RS from left to right in Fig. 3a) [38]. Zone I is a heat affected zone (HAZ), formed from a partially melted region of the two-phase microstructure of the nanocrystalline Al-10Cu [33,38]. Zone II is a transition region where the pro-eutectic α-Al phase underwent transitions from planar to cellular and then to dendritic growth mode, and θ-Al_2Cu formed from Cu-enriched liquid in intercellular and interdendritic regions at the onset of directional RS. After further acceleration of the solidification interface Zone III formed by a transition from dendritic to cellular growth mode and comprises columnar morphology grains with a matrix lattice of α-Al supersaturated solid solution and mostly discontinuously distributed θ'-Al_2Cu phase [30,33,38]. Zone IV is formed by several banded morphology grains that originated from select columnar morphology grains of zone III as the solidification interface conditions reached locally critical conditions for a final growth mode change [30,33,38]. Banded grains exhibit alternating single-phase bands of maximally supersaturated α-Al and two-phase bands of α-Al and discontinuous θ'-Al_2Cu [30,33,38].

Representative sections of the RS microstructure at location B (Fig. 2a), which was formed by two laser pulses, a first higher energy pulse of 0.86 μJ and second lower energy pulse of 0.6 μJ (Fig. 2b), is shown in Fig. 3b. The first pulse established a large melt pool of comparable

dimensions to that observed in Fig. 3a. Associated RS microstructure zones formed by the initial transient in the RS microstructure at location B (Fig. 2a) are marked in yellow labels as zone I, II, and III in Fig. 3b. In response to the second lower energy (0.6 μJ) laser pulse a second melt pool formed from regions of RS microstructure that included zone IV and parts of zone III established in the first transient (label 2nd melt pool, Fig. 3b). This was unexpected, since the energy of the second laser pulse, 0.6 μJ, was selected to be smaller than the threshold energy for melting of 0.7 μJ determined for the nanocrystalline as-deposited state (see section 2).

The reduced amount of photon energy of the second laser pulse generated sufficient enthalpy in the central regions of the coarsened and morphologically altered RS microstructure regions of the columnar grains in zone III and the banded grains in zone IV to result in complete and partial melting (labels second melt pool and 2nd HAZ, Fig. 3b). This observation can be rationalized either by reduced optical reflectivity caused by the microstructural characteristics of the RS microstructure, a local reduction of the alloy layer thickness due to mass losses during the prior pulse of laser irradiation (e.g., via evaporation) or a combination of both. In the case of reduced thickness of the alloy layer, i.e., mass loss, the total enthalpy (heat) required to melt is reduced, which then results in a lower threshold energy for the laser pulse to induce melting. If the coarsening of the microstructural scale and the morphology changes of the RS microstructure reduced the optical reflectivity relative to the nanocrystalline state the fraction of incident photon energy of the laser pulse that is converted to heat (enthalpy) in the alloy layer increases, and the nominally sub-threshold energy of the second laser pulse could have deposited sufficient enthalpy for melting during the second transient (Fig. 2b, panel B).

The smaller second melt pool resolidified to form RS microstructure with all four of the characteristic regions of zones I, II, III and IV (blue double-headed arrows, Fig. 3b). The second thermal transient also produced coarsening of the microstructure of the columnar grains of zone III established in the first transient that surrounds the second melt pool (Fig. 3b). This is particularly noticeable in regions directly adjacent to the 2nd HAZ formed during the second transient (labels cont. θ' and 2nd HAZ, Fig. 3b). The scale of the two-phase microstructure in zone I and zone II formed for the second melt pool appears to be coarsened relative to the scale of the equivalent zones I and II established in the initial thermal transient induced by the first laser pulse (Fig. 3b). This is consistent with the expected Gaussian thermal profiles resulting from the laser irradiation pulses and effects of the scale of the columnar grains of zone III of the RS

microstructure, which has significantly coarsened relative to the nanocrystalline state of the as-deposited microstructure, on the epitaxial growth from solid phases retained at the solid-liquid interface at the onset of directional RS [48].

The RS microstructure shown in Fig. 3c is a representative section of location C in Fig. 2a, which was also created by two thermal transients induced by a first high energy, 0.86 μJ, and second lower energy, 0.56 μJ, laser pulse (see Fig. 2). Comparing the RS microstructures in Fig. 3a and Fig. 3c enables assessment of the effects of non-isothermal annealing by the second laser pulse since, unlike in the case of the RS microstructure shown in Fig. 3b, the second pulse did not induce local melting for the laser irradiation sequence applied to location C. The second laser pulse generated a Gaussian thermal profile with highest temperatures in the center of the RS microstructure established by the initial transient of the first laser pulse. Hence, the non-isothermal annealing effects from the second thermal transient are most significant for the banded grains of zone IV. The non-isothermal annealing resulted in considerable coarsening and coalescing of the originally nanometer scale, spheroidal shaped, and discontinuously distributed θ'-Al_2Cu phase in the two-phase bands of the zone IV grains and the columnar grains of zone III. While remnant signatures of the banded morphology remain, single-phase and two-phase bands are no longer clearly discernible in zone IV after the single non-isothermal annealing transient caused by the second laser pulse (label IV, Fig. 3c). The non-isothermal annealing also induced significant changes in the columnar grains of zone III (Fig. 3a, Fig. 3c, label III). The θ'-Al_2Cu phase coarsened and formed an increasingly interconnected, continuous network within the α-Al matrix as the boundary between zone III and zone IV is approached (Fig 3c). In the immediate vicinity of the boundary between zones III and IV, the intercellular/intergranular boundaries are difficult to detect for the columnar grains of zone III and the microstructures in zone III and IV have essentially the same morphology and scale (Fig. 3c). Zone III of the annealed RS microstructure shown in Fig. 3c is divided into a region labeled discontinuous θ' and continuous θ' to indicate a lack of discernible effects and the presence of the significant morphological and scale modification in response to the non-isothermal annealing transient from the second laser pulse for the former and latter, respectively.

The RS microstructure of location D in Fig. 2a is the result of three laser pulses with energies of 0.86 μJ for the first transient and then 0.56 μJ for the second and the third transients (Fig.3d). Akin to the case of the MM-DTEM experiment described in Fig. 3b, melting of central

regions associated with parts of RS microstructure zones III and IV formed by the first and second transients resulted during the third transient. The second melt pool formed in the RS microstructure at location C in response to the application of the third laser pulse is larger than that formed for the higher energy second laser pulse, 0.6 μJ, applied to the RS microstructure at location B (Fig. 3b and Fig. 3d). The non-isothermally annealed RS microstructure shown in Fig. 3c would be expected to be a fair representation of the state prior to the third transient experienced by the microstructure shown in Fig. 3d. After non-isothermal annealing zone III and zone IV of the RS microstructures exhibited significantly coarsened scales of the secondary Al_2Cu phase related constituents (Fig. 3a and Fig. 3c). The increased size of the second melt pool formed in Fig. 3d relative to that in Fig. 3b would be consistent with the hypothesis that temperatures sufficient for melting can be achieved for smaller laser pulse energy as the RS microstructure of the Al-10Cu alloy coarsened in response to laser pulses and associated non-isothermal annealing during the second transient. The RS microstructure established for the second melt pool shown in Fig. 3d also shows the four distinct zones I, II, III, and IV (labels 2^{nd} HAZ, II, III, IV and 2^{nd} melt pool, Fig. 3d). The width and the scale of the microstructural features of the 2^{nd} HAZ regions formed at the perimeter of the second melt pools in the RS microstructures shown in Fig. 3b and Fig. 3d are essentially identical.

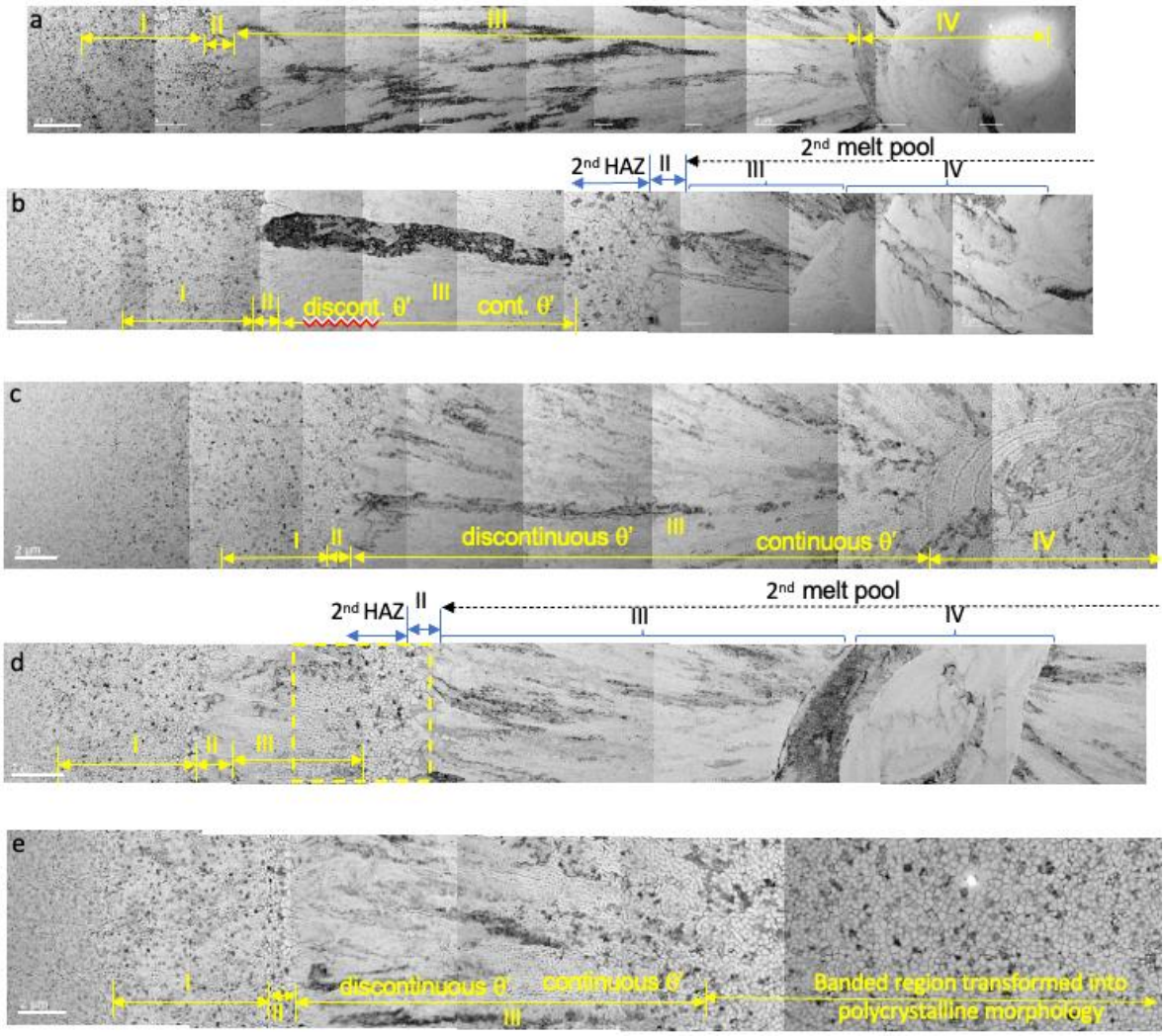

Fig. 3: Montages of BF STEM images showing the morphologically distinct regions, marked by labels I, II, III and IV, characteristic of the RS microstructures of the Al-10Cu alloy after the different pulsed laser irradiation schemes applied to locations marked A to E in Fig. 2. Sections in a) from location A, single laser pulse for melting, b) from location B, two laser melting pulses of different energy, c) from location C, single laser pulse for melting and one subsequent laser pulse for annealing, d) from location D, single laser melting pulse and two subsequent annealing laser pulses, and e) for location E, laser melting pulses and three subsequent laser pulses for annealing. See online version of this article for color images and see text for more details.

Fig. 3e shows a representative section of the RS microstructure from location E in Fig. 2a, which was exposed to four laser pulse-induced thermal transients (Fig. 2b). The first laser pulse, 0.86 μJ, established the original RS microstructure with zone I, II, III, and IV in the initial transient involving the solid-liquid-solid transformation sequence. Subsequently, the second laser pulse, 0.56 μJ, third and fourth pulses, 0.5 μJ, imposed non-isothermal transients. Fig. 3a and Fig. 3c can

be considered reasonable representations of the nonequilibrium features in the microstructures of the Al-10Cu alloy encountered after the first and second laser pulses, respectively. Relative to the effects of the single non-isothermal annealing transient on the RS microstructure shown in Fig.3c, the three non-isothermal annealing pulses resulted in a broadening of the regions of the columnar grains of zone III that exhibited further coarsened scale and coalescence of the θ'-Al_2Cu phase, establishing the regions marked as continuous θ'-phase in Fig. 3e. Furthermore, the central regions of the melt pool induced by the first laser pulse and originally associated with the banded grains of zone IV in the RS microstructure after the initial transient changed in morphology to resemble that of the 2nd HAZ observed in Fig. 3d with coarsened Al grains of equiaxial shape surrounded by a continuous network of Al_2Cu phase (Figs. 3a, 3c, 3d and 3e). Prior studies have shown that the HAZ microstructures formed from partially melted regions of the as-deposited hypoeutectic Al-Cu alloy film [33,38]. It is therefore plausible to propose that the fourth laser pulse resulted in partial melting for the central region of the coarsened and morphologically altered zone IV of the original RS microstructure established by the non-isothermal annealing during the second and third transients (Fig. 3e).

After the initial transient that established morphologically distinct regions of the RS microstructure, a stepwise progression of the nonequilibrium features in response to repeated non-isothermal annealing transients induced by sequences of laser pulses can be inferred from comparison of equivalent regions of the microstructures in Fig. 3a, Fig. 3c, and Fig. 3e. In the RS microstructure of the Al-10Cu alloy (e.g., Fig. 3a), the banded region of zone IV with its alternating single-phase and two-phase bands formed under conditions driven the farthest away from equilibrium, while the HAZ microstructure of zone I formed under conditions driven the least away from equilibrium. If melting is avoided, each subsequent non-isothermal annealing transient evolves the non-equilibrium features of the RS microstructure stepwise closer towards equilibrium configurations (Fig. 3a. 3c and 3e).

3.2.2 PED TEM mapping of the non-isothermally annealed RS microstructures

Considering the Gaussian shape of the thermal profiles developing after each laser pulse in the irradiated region of the Al-10Cu, the central regions of the RS microstructure (e.g., zone IV) experience excursions to higher temperatures than the peripheral regions of zone I during each thermal transient. Hence, the relatively minor changes for zone I and the comparatively drastic

changes observed for zone IV regions of the original RS microstructure can be attributed to the Gaussian laser beam profile (e.g., Fig. 3a, 3c, and 3e). The changes observed in the RS microstructure for laser pulse sequences with non-isothermal transients that avoided local melting can be expected to be consistent with non-steady state solid-solid transformation processes facilitated by Cu solute diffusion, reducing the level of supersaturation of the Al solid solution and resulting in growth and nucleation of the Cu-rich phases of thermodynamically metastable θ'-Al_2Cu and stable θ-Al_2Cu. To determine orientation and phase changes key sections of the RS microstructures developed at locations C, D, and E were characterized by PED-ACOM TEM (Figs. 4, 5, and 6) [37], [49]. The inverse pole figure (IPF) based orientation maps display the phase-specific crystal lattice directions parallel to the incident electron beam direction (Figs. 4, 5, and 6).

3.2.2.1 Banded regions after a single non-isothermal annealing transient

Results from PED-ACOM of non-isothermal annealed banded grains of zone IV after application of two laser pulses at location C are shown in Fig. 4. Two prominent banded grains are marked as 1, 2 in the BF STEM image of Fig. 4a and in the phase map of Fig. 4b. For convenience parts of the adjacent zone III region of columnar grains are also marked, label III, Fig. 4a. Before carrying out the PED-ACOM, the banded grain labeled 1 was aligned closely toward the [001] zone axis of the Al matrix lattice by tilting the sample holder. Fig.4b and Fig. 4c show the phase map and orientation map of the region marked by the rectangle in Fig. 4a. In addition to the α-Al (red) and θ'-Al_2Cu (blue), formation of limited amount of isolated patches of θ-Al_2Cu (green) is evident in Fig. 4b. Prior reports have demonstrated that the two-phase bands of the banded morphology grains of zone IV in the RS microstructures of hypoeutectic Al-Cu alloys consist only of α-Al and θ'-Al_2Cu phases, while the single phase bands are comprised of supersaturated α-Al with nanometer scale clusters exhibiting structure resembling θ'-Al_2Cu of on average 2-3nm in size [33,36,38]. Therefore, the phase map of Fig. 4b confirms nucleation and growth of stable θ-Al_2Cu and coarsening and coalescence of pre-existing θ'-Al_2Cu during the single non-isothermal annealing transient imposed by the second laser pulse for the banded grains of the original RS microstructure established by the initial transient (Fig. 4b).

Formation of θ-Al_2Cu (green, Fig. 4b) is also detected for some locations in zone III of the RS microstructure adjacent to the banded grains of zone IV (Fig. 4a, 4b). Furthermore, the phase map clearly shows that in the banded grain marked by the label 2 in Fig. 4a and 4b, which is titled slightly away from the [001] zone axis orientation of the Al matrix lattice, the θ'-Al_2Cu phase (blue) has formed a continuous network (Fig. 4b). Prior to the non-isothermal annealing θ'-Al_2Cu presented in the banded grains as spheroidal shapes with dimensions of ≈ 15 to 30 nm along minor and major diameters that were discontinuously distributed and enveloped by the α-Al matrix lattice in the two-phase bands [33,36,38]. θ'-Al_2Cu phase forming in solid-solid transformation by precipitation reactions tend obey a "cube-on-cube" orientation relationship with the Al matrix

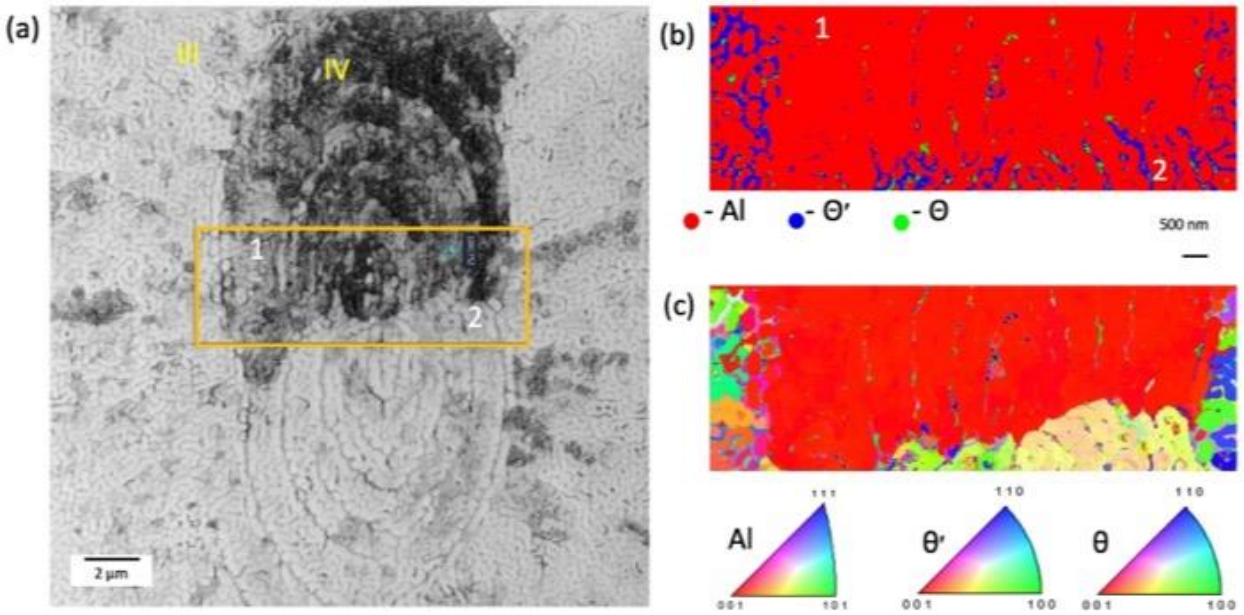

Fig. 4: Banded region of the RS microstructure, zone IV, after a single annealing pulse application shown in the center of Fig. 3c. a) BF STEM image, b) phase map and c) orientation map for region marked by rectangle in a). Color-coded phase and orientation legends for b) and c) are shown. Directions plotted in c) are parallel to the incident electron beam direction. In a) two prominent banded morphology grains are marked by the labels 1 and 2, and labels III and IV mark the columnar grain and banded grain regions. See online version of this article for color images.

lattice, [001]θ' || [001]α and {100}θ' || {100}α [50]. This permits coherent interfacial structure formation to reduce interfacial free energy and the activation barrier for nucleation and results in development of plate or disc shapes during growth due to crystallographic constraint and effects from interfacial strain energy [50]. While also typically obeying the "cube-on-cube" orientation relationship, the spheroidal shapes of the θ'-Al_2Cu observed in the RS microstructure after the

initial transient demonstrate that they formed during the solidification process from the liquid [33,36,38]. The alignment of the α-Al matrix lattice of the banded grain labeled 1 with the [001] direction leads to strong diffraction patterns from this phase (red color in Fig. 4b). This consistently obscures detection of the weaker diffraction signals from the nanoscale Al_2Cu phases that are embedded within the continuous α-Al matrix for the banded grain labeled 1 in Fig. 4b. Hence, due to their small size and crystallographic orientation relationship with the Al matrix the presence of the Al_2Cu phases remains under-detected in the PED-ACOM phase map [49]. For the banded grain labeled 2 in Fig. 4 the slight misalignment away from the high-symmetry [001] orientation of the matrix lattice enhances the probability for detection of Al_2Cu phases in the PED-ACOM experiments [49]. The BF image, Fig.4a, clearly shows continuous θ'-Al_2Cu in the banded grain region as well as in the columnar grain region (e.g., labels IV and III, Fig. 4a). In response to the single non-isothermal annealing transient imposed by the second lower energy laser pulse θ'-Al_2Cu phase has coarsened and coalesced to form a more continuous network and some transformation to stable θ-Al_2Cu phase occurred within the banded grain region of zone IV of the RS microstructure (Fig. 3a, Fig. 3c, Fig. 4).

3.2.2.2 Laser pulse induced remelting of RS microstructure

A second smaller melt pool developed in the central region for the RS microstructure at location D during the laser irradiation induced sequence of three thermal transients. The smaller secondary melt pool region re-solidified to establish the same four characteristic morphologically distinct zones observed after the initial melting transient (e.g., compare region marked 2^{nd} melt pool in Fig. 3d with Fig. 3a). PED-ACOM was carried out for a region at the boundary of the secondary melt pool with the non-isothermally annealed microstructure. This region of the RS microstructure included sections of columnar grains of zone III developed from the primary melt pool (e.g., yellow labels and arrows, Fig. 5a), and the 2^{nd} HAZ, the transition region, zone II, and parts of the columnar grains of zone III (e.g., black labels and blue arrows, markers, Fig. 5a), respectively, developed from the secondary melt pool (Fig. 5). Fig. 5b shows the phase map and Fig. 5c the orientation map for the selected scan area marked by the rectangle inset to the STEM image of Fig. 5a. The phase map shows the presence of three phases, namely, α-Al (red), θ'-Al_2Cu (blue), and θ-Al_2Cu (green)) (Fig. 5b). Formation of the θ-Al_2Cu phase is evident inside the columnar grains of zone III developed from the primary melt pool and in the intercellular/intergranular

regions separating them (Fig. 5b). According to the PED-ACOM phase maps, the area fraction of θ-Al_2Cu phase inside the zone III grains formed by RS of the primary melt pool increases as the distance to the boundary with the 2nd HAZ decreases (black arrow and label III, Fig. 5b). This is consistent with the Gaussian thermal profile associated with the laser irradiation pulses. Volume

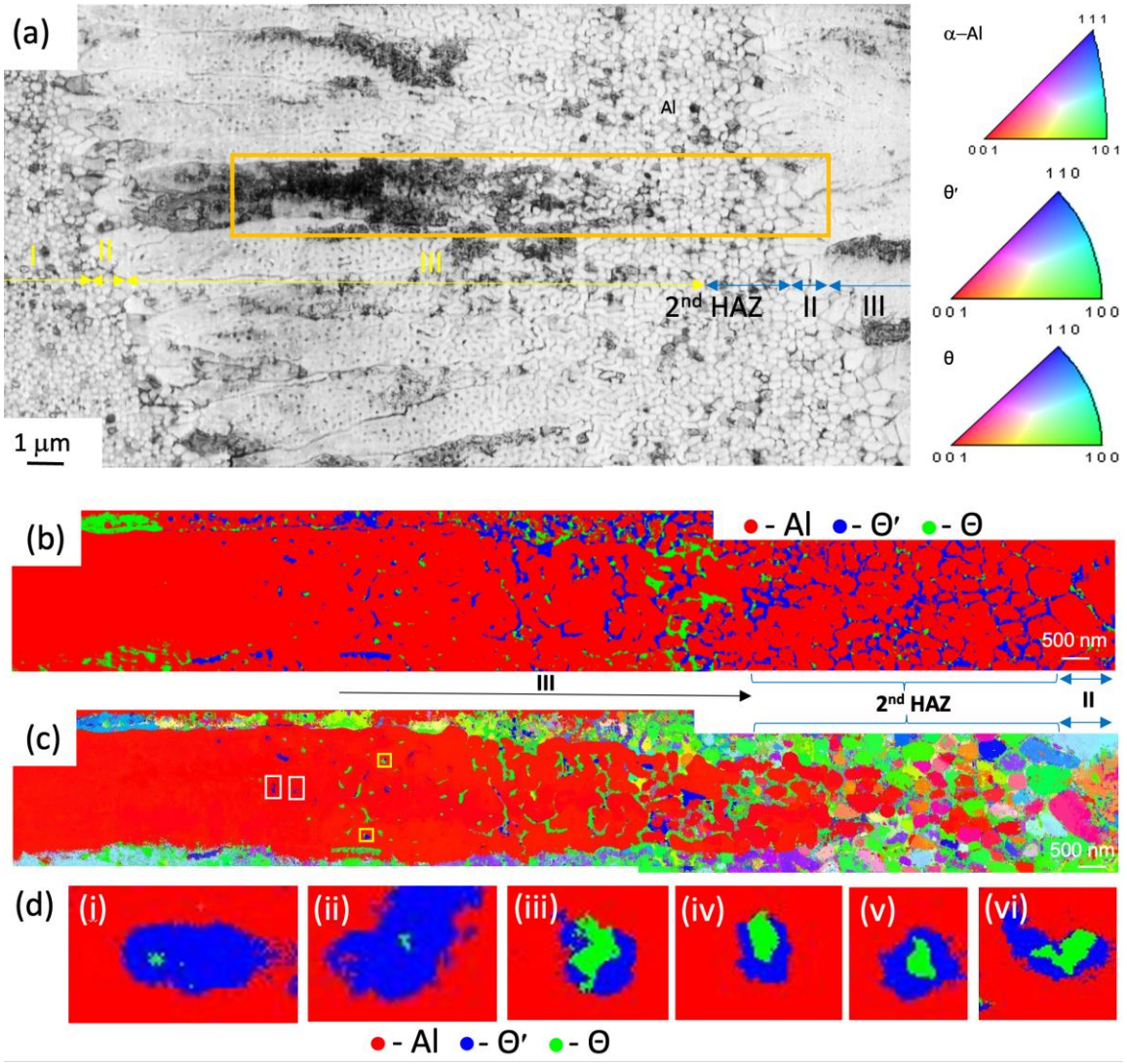

Fig. 5: Higher magnification details of the RS microstructure at the edge of the second smaller melt pool in the center of the laser irradiated region marked D in Fig. 2a and shown at lower magnification in Fig. 3d. (a) BF STEM image, (b) phase map for region, and (c) inverse-pole-figure based orientation map of the direction parallel to the incident electron beam (normal to paper plane) for the region marked by the rectangle in (a). (d) Select examples at higher magnification extracted from phase map in (b) of θ'-phase transforming to θ-phase. Color-coded phase and crystal orientation legends are shown. See online version of this article for color images.

elements located more centrally in the RS microstructure experience larger temperature excursion during the laser pulse induced transients and maintain elevated temperatures conducive to facilitation of significant diffusion rates for Cu and Al than those located more peripherally.

The orientation map (Fig. 5c) shows that θ'-Al_2Cu phase particles present in three orientations [001] (Red), [100] (Green), and [110] (blue). Examples of the PED patterns obtained for voxels from θ'-Al_2Cu phase particles that have been indexed as the three distinct orientations in Fig. 5c are shown in Fig. 6b and Fig. 6c, respectively. The PED patterns of the α-Al columnar matrix grain with [001] orientation (Fig. 6a) and those of two different orientations of θ-Al_2Cu phase particles (Fig. 6d and Fig. 6e) are also shown. Notably, the PED patterns for θ'-Al_2Cu phase particles indexed as red and those indexed as blue in the orientation maps (e.g., Fig. 5c) were found to be identical (Fig. 6b), while θ'-Al_2Cu phase particles indexed as green exhibited consistently a distinct type of PED pattern (Fig. 6c). The first types of electron diffraction patterns, e.g., Fig. 6b, have been indexed via the template matching approach used by the PED analysis software with two different orientations at different regions within the RS microstructure. For some regions this type of PED pattern is indexed with [001] (red) and for some other regions it is indexed with [110] (blue). To elucidate the reason for the indexing of this type of PED pattern with the two different orientations of θ'-Al_2Cu, computer simulations of electron diffraction patterns have been performed for the three phases (α-Al, θ'-Al_2Cu, and θ-Al_2Cu) presenting in the RS microstructure of Fig. 5a using the JEMS software package [51,52]. Computed electron diffraction patterns that match the respective experimental electron diffraction patterns are shown in Fig. 6. Note the relative rotation by ≈26˚ about the respective ZA direction between computed and experimental electron diffraction patterns, e.g., for the reference [001] ZA patterns of the α-Al matrix in Fig. 6a. Since the magnitudes for the crystallographic nonequivalent diffraction vectors $\mathbf{g}_{002}$ and $\mathbf{g}_{-110}$ differ by about 1.5% and those for $\mathbf{g}_{020}$ and $\mathbf{g}_{-112}$ by only about 0.75% for θ'-Al_2Cu, the computed electron diffraction patterns for the four-fold rotational symmetry [001] and two-fold rotational symmetry [110] ZA orientations shown below the experimental pattern in Fig. 6b closely resemble each other. This introduces ambiguity to the results of the reciprocal lattice template matching routines used for orientation determination [49]. Hence, the absolute best match resulted for the θ'-Al_2Cu experimental diffraction patterns of the type shown in Fig. 6b for indexing with [001] (red) in some regions and with [110] (blue) in some other regions.

The OR between the α-Al matrix lattice and θ'-Al_2Cu phase resulting from precipitation during the annealing of supersaturated solid solutions in Al-Cu alloy (i.e., entirely via solid-state phenomena) is energetically favored to be of cube-on-cube type, which can be described as

$\langle 001\rangle_{\theta'} \,||\, \langle 001\rangle_{\alpha}$ and $\{100\}_{\theta'} \,||\, \{100\}_{\alpha}$ [50].

In the orientation map of Fig. 5c the α-Al matrix reference direction plotted is the normal to the image plane and is oriented along [001] orientation. Based on the cube-on-cube OR the equivalent direction for the θ'-Al_2Cu should also be along [001] (red, Fig. 5c) or along [010] (green, Fig. 5c) or [100] (also green, Fig. 5c). Notably, the second types of electron diffraction pattern consistently observed for the θ'-Al_2Cu phase particles (i.e., those indexed as green and shown in Fig. 6c) match with the [100] ZA computed electron diffraction pattern. This confirms the orientation of θ'-Al_2Cu phase particles with green color indexing in the orientation map of Fig. 5c as [100] or equivalently [010]. The respective OR between α-Al (red) and θ'-Al_2Cu (green) in the orientation map of Fig. 5c can be described for them as $[100]_{\theta'} \,||\, [001]_{\alpha}$ and $(002)_{\theta'} \,||\, (020)_{\alpha}$.

In cube-on-cube OR the three orientation variants of θ'-Al_2Cu have their c-axis parallel to one of the three cubic <100> directions of α-Al. The OR determined for the green color indexed θ'-Al_2Cu particles identifies them as a second orientation variant consistent with the cube-on-cube OR. The pulsed laser induced thermal transients resulted in coarsening and phase transformation of the θ'-Al_2Cu that formed from the liquid state during RS, which is accomplished by solid-state processes (e.g., Fig. 4, Fig. 5b). During solid-state transformations the cube-on-cube OR for α-Al and θ'-Al_2Cu is energetically favored over other possible OR's, e.g., the unusual non-cube OR that would be equivalent to the case of the blue indexed θ'-Al_2Cu in Fig. 5c. This unusual non-cube OR is illustrated as the 45˚-rotated option in the computed electron diffraction patterns shown in Fig. 6b with respect to the computed electron diffraction pattern of the α-Al reference lattice shown in Fig. 6a and can be described as $[001]_{\alpha} \,||\, [110]_{\theta'}$ and $(110)_{\alpha} \,||\, (\bar{1}10)_{\theta'}$. Therefore, we conclude that the coarsened θ'-Al_2Cu observed after pulsed laser irradiation induced thermal transients in the RS microstructure of the Al-10Cu alloy conform with the cube-on-cube OR and the PED pattern indexing software routines erroneously indexed some of the [001] diffraction patterns of the θ'-Al_2Cu phase with [110] (blue) orientation. In the rest of the manuscript θ'-Al_2Cu

phase indexed with [110] (blue) orientation in the PED based orientation maps (e.g., Fig. 5c) is considered as [001] (red) orientation, consistent with a cube-on-cube OR with the α-Al matrix.

Fig. 5d displays example sections extracted from the phase map of Fig. 5b that illustrate θ-Al_2Cu phase formation at the interface of the coarsened θ'-Al_2Cu that are distributed discontinuously in the α-Al matrix of the columnar grains of zone III in the RS microstructure. Some of them are highlighted by smaller yellow and white boxes in the orientation map of Fig. 5c, respectively. The θ-Al_2Cu precipitates have nucleated within and at the interface of θ'-Al_2Cu particles with the α-Al matrix. θ-Al_2Cu particles that have nucleated at the [001] (red, blue θ'-phase, Fig. 5c) and [100] (green θ'-phase, Fig. 5c) oriented θ'-Al_2Cu particles have [001] (red) and [110] (blue) orientation, respectively (e.g., small white and yellow boxes, respectively, marked in Fig. 5c and equivalent locales in phase maps of Fig. 5b, and Fig. 5d). This is consistent with the

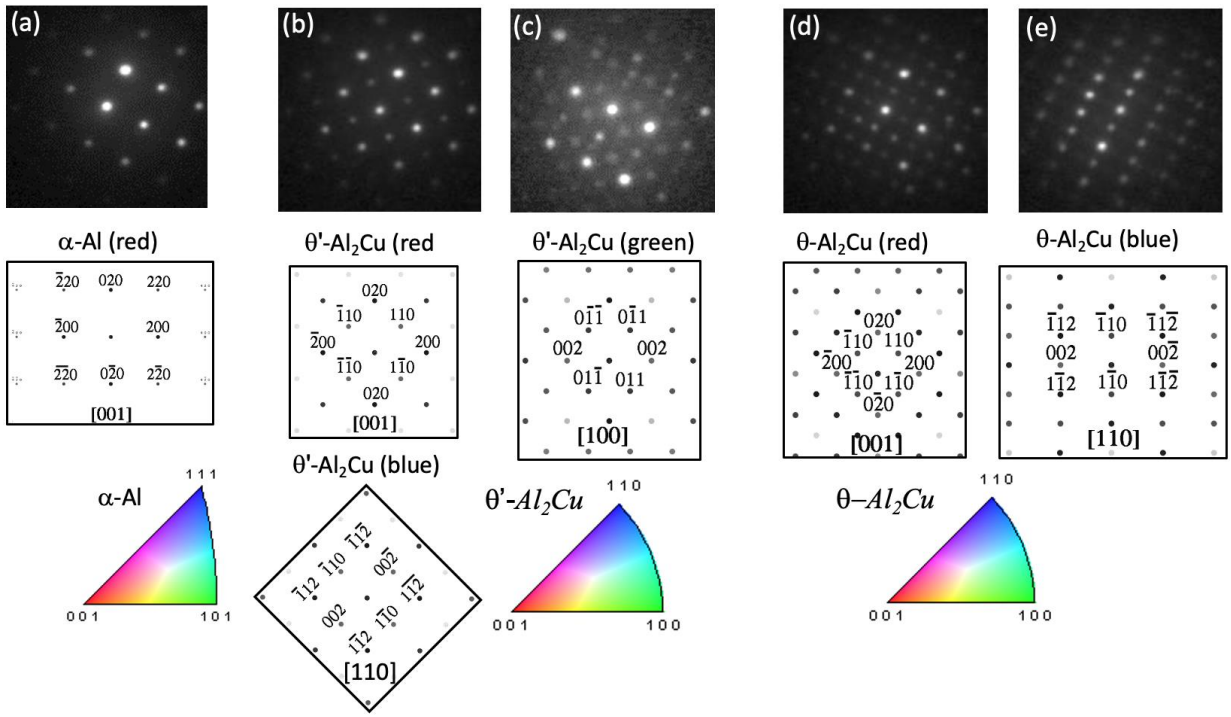

Fig. 6: Comparison of experimental PED patterns and matching computed electron diffraction patterns for a) the [001] zone axis orientation of the α-Al matrix phase, and b) and c) the secondary θ'-Al_2Cu phase orientation variants, and d)and e) the θ-Al_2Cu phase detected in the PED ACOM orientation and corresponding phase mappings shown in Fig. 5. Color-coded crystal orientation legends are shown for each phase. See online version for color images.

presence of the different orientation variants of θ'-Al_2Cu particles presenting in the non-

isothermally annealed RS microstructure with a cube-on-cube OR with respect to the α-Al. Two different and orientation variant dependent ORs for the three phases can be identified and are described as follows:

$$[001]_{\alpha} \,||\, [001]_{\theta'} ||\; [001]_{\theta} \text{ and } (110)_{\alpha} \,||\; (110)_{\theta'} \,||\; (100)_{\theta}$$

$$\text{and } [001]_{\alpha} \,||\; [100]_{\theta'} \,||\; [110]_{\theta} \text{ and } (020)_{\alpha} \,||\; (002)_{\theta'} \,||\; (1\bar{1}0)_{\theta}$$

Mechanisms for heterogeneous nucleation of θ-Al_2Cu at the interface between θ'-Al_2Cu and α-Al phase have been proposed by Laird et al. [21], which would result in θ-Al_2Cu with a Guinier-I orientation relationship with the α-Al phase. The ORs observed here (e.g., Fig. 5, Fig. 6) match with the Guinier-I OR and are therefore consistent with the mechanisms for heterogenous nucleation reported by Laird et al. [21].

Morphologically the microstructure of the 2nd HAZ is equivalent to that of the HAZ (zone I) formed by solidification of a partially melted region resulting from the first laser pulse of the irradiation sequence at the perimeter of the through-thickness melt pool (e.g., Fig. 3d). Interestingly, for the 2nd HAZ the θ'-Al_2Cu formed a continuous network separating the equiaxed α-Al grains (Fig. 5b). In contrast, for the HAZ developed from the nano-crystalline as-deposited Al-10Cu during the initial transient the thermodynamically stable θ-Al_2Cu phase presented as the continuous network between the α-Al grains [30,33,38]. The as-deposited Al-10Cu was comprised of α-Al and θ-Al_2Cu phase, while the RS microstructure zone III is comprised of θ'-Al_2Cu phase and α-Al (Fig. 1, Fig. 3d, Fig. 5b). Hence, the θ'-Al_2Cu formation in the 2nd HAZ is attributed here to seeded growth from the zone III RS microstructure during re-solidification of the partially melted regions resulting from the third laser pulse irradiation induced thermal transient. The phase-specific crystal orientation map clearly shows a change in the local texture of the α-Al grains in the 2nd HAZ (Fig. 5c). The equiaxial α−Al grains in the left-hand-side part of the 2nd HAZ exhibit [001] orientation (red color, Fig. 5c), while those located closer to the boundary with the transition region, marker II in Fig. 5a, have developed a wider spread of orientations (other colors than red presenting, Fig. 5c).

The formation of θ-Al_2Cu and the characteristics of the 2nd HAZ observed after multiple non-isothermal transients for the RS microstructure near location D are consistent with the Gaussian temperature profile generated in the final transient associated with the third laser pulse.

With reference to Fig. 5b and Fig 5c, the average and the maximum temperature reached during the third and final transient increased from the left to the right.

For locations to the right of the 2nd HAZ (i.e., in the transition region, zone II) the temperature exceeded the melting temperatures for the supersaturated Al and the Al_2Cu phases for sufficient time to melt the entire thickness of the alloy layer during the third laser pulse induced non-isothermal transient (right-hand-side of 2nd HAZ, label II, Fig. 5). Zone II, III, and IV RS microstructure developed here from the smaller secondary melt pool via epitaxial growth seeded by the solid that formed at the boundary between the 2nd HAZ and zone II (Fig. 3d, Fig. 5).

To the left of the 2nd HAZ in the columnar grains of zone III of the RS microstructure presenting after the second transient, the temperatures reached during the third transient remained below the phase-specific melting temperatures and microstructural changes involved only solid-solid transformations. For the uniformly red colored regions at the left-hand-side of Fig. 5b and Fig. 5c the exposure time to sufficiently elevated temperatures during the second and third non-isothermal transients did not produce enough coarsening of the nanoscale intragranular θ'-Al_2Cu to render their sizes readily detectable in the PED-ACOM analysis (Fig. 5b). The regions closer to the center of the irradiated area (i.e., the zone III regions nearer the boundary with the 2nd HAZ in Fig. 5) experienced larger maximal temperature and were exposed for longer durations to supercritical temperatures required for more significant solute and solvent atom mobility by lattice diffusion. Consequently, coarsening of the intra- and intergranular θ'-Al_2Cu phase and nucleation and growth of θ-Al_2Cu phase to a scale sufficient for detection in the PED-ACOM occurred during the third transient for locations in columnar grains of zone III at locations closer to the 2nd HAZ (Fig. 5b). The area fraction of θ-Al_2Cu increased from left-to-right in the columnar grains of zone III correspondingly with the increase in the maximum temperatures established by the third laser pulse (Fig. 5b).

In the 2nd HAZ the average and maximum temperatures reached during the third non-isothermal transient also increased from left to right and to higher temperatures than in the columnar grains of zone III to their left (Fig. 5). The 2nd HAZ formed from a partially melted region established during the third transient from the annealed columnar grains in zone III of the RS microstructure established after the first two laser pulses, e.g., Fig. 3c and Fig. 4 [30,33,38]. At the left-hand side of the 2nd HAZ the non-isothermal exposure during the third transient was sufficient to melt partially the coarsened and coalescing θ'-Al_2Cu and newly formed θ-Al_2Cu,

which have lower liquidus temperatures than the annealed Al solid solution and were established in response to the second transient. The Al phase remained solid through the thickness of the film in the left-hand-side parts of the 2nd HAZ (red color in Fig. 5b) and therefore retained the same crystal orientation as the Al matrix in the adjacent columnar grains of zone III of the RS microstructure (Fig. 5b). Seeded growth during re-solidification of the at least partially melted Al_2Cu phases resulted in formation of the continuous network of predominantly θ'-Al_2Cu enveloping the Al grains of the 2nd HAZ (Fig. 5b). The fraction of liquid phase developing during the third transient increased from left-to-right in the 2nd HAZ (Fig. 5). On the right-hand-side of the 2nd HAZ the third transient provided sufficient thermal exposure to fully melt the Al_2Cu phases and partially melt the Al phase. Given that the Al_2Cu phase had coarsened and by coalescing formed a more continuous arrangement in response to the second non-isothermal transient exposure (e.g., zone III in Fig. 3c, Fig. 4, Fig. 5) it can be envisaged that this resulted in temporary existence of separate grains of retained Al surrounded by liquid of Cu-enriched composition relative to the alloy during the third transient. If this were the case, these retained grains of Al solid would be free to reorient prior to re-solidification during the cooling section of the third non-isothermal transient. While hypothetical, the proposed scenario would be suitable to rationalize the observed changes in lattice orientations for the α-Al phase regions in the 2nd HAZ, which changes from a preferred [001] alignment approximately parallel to <001> (red color, 2nd HAZ left-side, Fig. 5c) to a wider range of orientations (multiple colors, 2nd HAZ center and right-side, Fig. 5c). Since the microstructural morphology observed for the central region of the RS microstructure observed after four laser pulse irradiations at location E resembled that of the 2nd HAZ formed in the RS microstructures generated at locations B and D (Fig. 3b, Fig. 3d and Fig. 3e) PED-ACOM TEM analysis has been performed also for this region.

3.2.2.3 Banded regions after multiple non-isothermal annealing transients

Fig. 7 shows a BF-STEM image and corresponding PED-ACOM phase and orientation mapping data for the center region of the RS microstructure that evolved in response to four non-isothermal transients at location E. Here banded grains of zone IV of the RS microstructure experienced three non-isothermal annealing transients, which modified the nonequilibrium features of the characteristic single- and two-phase bands, prior to the fourth and final transient induced by a laser pulse of identical energy and duration as applied for the prior second and third transients (Fig. 2e,

Fig. 3e). The phase map shows the presence of an essentially continuous network of θ'-Al_2Cu (blue, Fig. 7b) separating several considerably coarsened grains of α-Al (red, Fig. 7b), diameters ≈ 0.5 μm. Furthermore, formation of θ-Al_2Cu phase (green, Fig. 7b) from the θ'-Al_2Cu phase and inside α-Al grains is evident (Fig. 7b). The orientation map shows different orientations for the nearly equiaxial α-Al grains (Fig. 7c). The orientation map also indicates multiple orientations of the distinct θ-Al_2Cu phase crystals relative to the α-Al and the θ'-Al_2Cu phases (Fig. 7c). These microstructural characteristics resemble those observed and discussed for parts of the 2nd HAZ formed in the RS microstructure developed near location D (Fig. 3d, Fig. 5).

The banded regions developed by the first transient with the 0.86 μJ laser pulse in the Al-10Cu alloy characteristically comprised only two or three prominent banded grains, each with maximal linear dimensions of about 5-8 μm in size (e.g., Fig. 3a, Fig. 3c). After annealing during a second transient induced by a laser pulse of 0.56 μJ (e.g., Fig. 3c, Fig. 4) the banded grains of zone IV of the RS microstructure maintained a single crystal α-Al matrix lattice containing primarily θ'-Al_2Cu phase coarsened in size and coalescing with some localized transformation to θ-Al_2Cu (e.g., Fig. 4). At location E the second, third, and fourth thermal transients were induced by laser pulses with identical energy of 0.5 μJ, an about 10% reduction relative to the laser pulses with energy 0.56 μJ applied to the RS microstructure at locations C, D. It is therefore reasonable to expect that the second and third transients applied to the RS microstructure produced near location E in Fig. 2 resulted in non-isothermal annealing without inducing melting. This would have coarsened the multiphase microstructure comprised of a majority fraction of α-phase, decreasing fraction of θ'-phase, and increasing fraction of θ-phase with morphological characteristics akin to those shown to evolve in Fig. 3c and Fig. 4 for the zone IV region of the RS microstructure presenting after the first transient. As was the case for the multiple orientations presenting for the α-Al grains in the 2nd HAZ and discussed with reference to Fig. 5, the large, coarsened size and the multitude of different orientations for the α-Al grains depicted in Fig. 7 would be consistent with the temporary existence of a partially melted region that retained small fractions of solid grains of Al enveloped by a layer of Cu-enriched liquid during the final non-isothermal transient. This implies that the fourth laser pulse, energy of 0.5 μJ, resulted in partial melting for the central region of the RS microstructure after it underwent scale coarsening for the banded region, zone IV, in response to the previous transients. Since local thinning of the TEM

transparent region was not detected in our studies, it is reasonable to conclude that the increased coarsening of the microstructural scale appears to have further reduced the effective reflectivity of the Al-10Cu alloy for the near infrared wavelength laser irradiation.

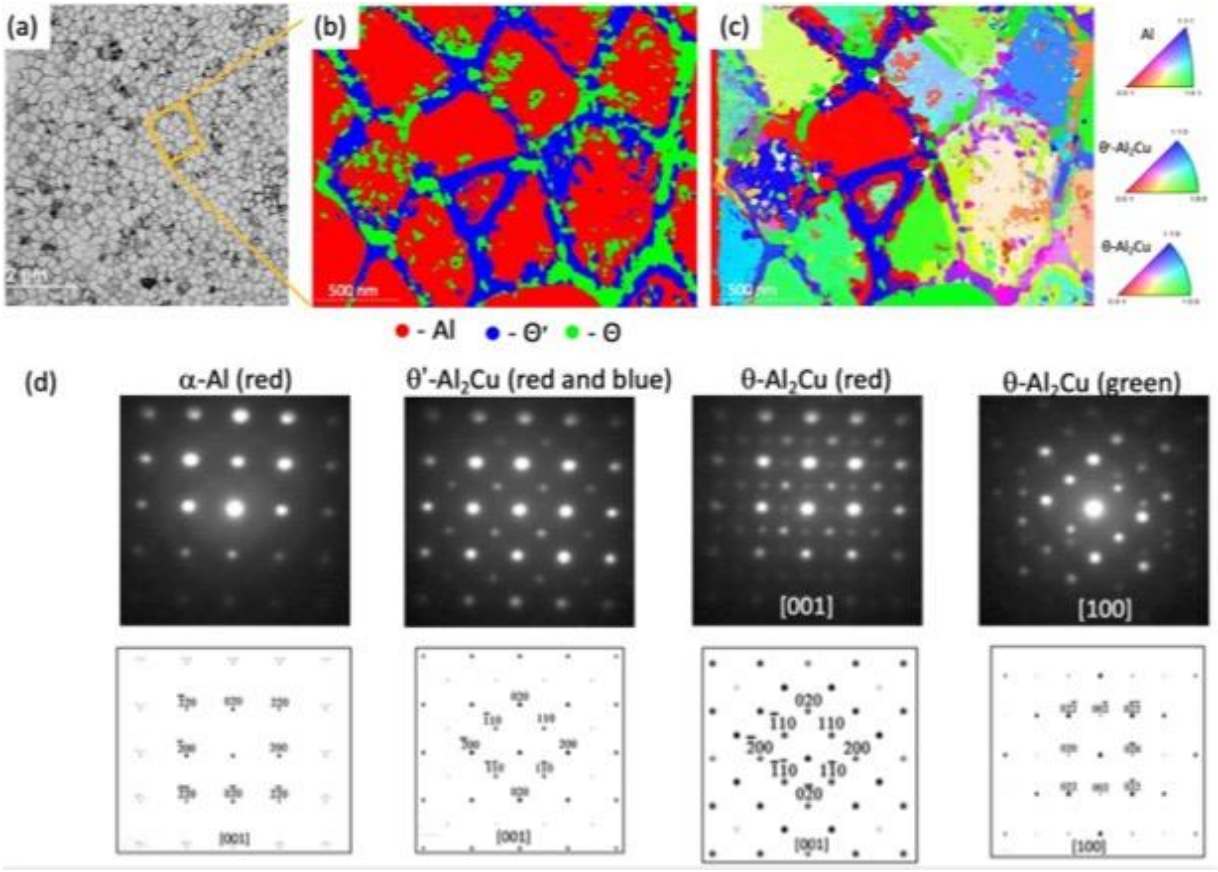

Fig. 7: Higher magnification details of the RS microstructure in the center of the laser irradiated region marked D in Fig. 2a) and shown as microstructure zone IV in Fig. 3e. a) BF STEM image, b) phase map and c) inverse-pole-figure based orientation map for the region marked by the rectangle in a) for the direction normal to the plane of the image. d) examples of experimental and matching computed electron diffraction patterns for the different phases. Color-coded phase and orientation legends for b) and c) are shown. (See online version for color.)

Multiple orientation relationships have been determined for the three phases that formed in response to the four non-isothermal transients for the RS microstructure established near location E shown in Fig. 2a, 3e, and Fig. 7 from the electron diffraction patterns extracted from the PED data (Fig.7). Examples of experimental and matching computed electron diffraction patterns for the dominant orientation relationships between α-Al, and the θ'- and θ-Al_2Cu phases have been determined as follows:

OR-1: $[001]_{\alpha} \,||\, [001]_{\theta'} \,||\, [001]_{\theta}$ and $(010)_{\alpha} \,||\, (010)_{\theta'} \,||\, (110)_{\theta}$

and

OR-2: $[001]_{\alpha}$ | | $[001]_{\theta'}$|| $[100]_{\theta}$ and $(\bar{1}10)_{\alpha}$ || $(\bar{1}10)_{\theta'}$|| $(001)_{\theta}$

The OR-1 and OR-2 are matches with the orientation relationships reported in prior works as Guinier I and Guinier II/III, respectively [19,21,29]. The presence of θ–Al_2Cu with OR-1 (Guinier I precipitates) is observed within the α-Al grains as well as in the θ'-Al_2Cu phase, whereas θ–Al_2Cu with OR-2 (Guinier II/III precipitates) is found consistently only adjacent to the θ–Al_2Cu with OR-1 phase regions, examples of which are marked by white arrows in Fig. 7c. The Guinier I precipitates of θ-phase can form via nucleation either in the α-Al matrix or in θ'-Al_2Cu precipitates [19,21]. Notably, Guinier I precipitates of θ-phase and OR-1 have also been observed for non-isothermally annealed columnar grains of the RS microstructure zone III (e.g., Fig. 5). The Guinier II/III precipitates of θ-phase have only been observed for the central region of the original RS microstructure where banded morphology grains (Zone IV, Fig. 3) transformed in response to multiple non-isothermal heating cycles and partial melting occurred (e.g., Fig. 7). Guinier II/III precipitates of θ-phase have not been detected for the non-isothermal states of the microstructurally distinct zones I, II, and III presenting in the original RS microstructure of the Al-10Cu alloy (e.g., Fig. 5). This dependence of the orientation of the θ–phase precipitates on the details of the structure of the sites for heterogeneous nucleation has been explained after observation in isothermally annealed bulk specimens by simple atomic matching between the respective two crystals [19,21]. In the present work, formation of Guinier I and Guinier II/III type orientation relationships has been determined to develop for θ-Al_2Cu relative to the α-Al matrix in the metastable nonequilibrium RS microstructures of Al-10Cu alloy during post-solidification non-isothermal annealing transients. This demonstrates that θ-Al_2Cu has formed via heterogeneous nucleation and subsequent growth from the θ'-Al_2Cu phase as well as the supersaturated α-Al matrix in response to the non-isothermal transients imposed by the sequences of nanosecond duration laser pulses.

4. Summary and Conclusions

Utilizing the in-situ pulsed laser irradiation capabilities of the MM-DTEM instrument and post-mortem analysis by TEM and STEM permitted an experimental study of the evolution of the multiphase RS microstructure of hypoeutectic Al-10Cu in response to sequences of rapid heating and cooling transients. The RS microstructure of the Al-10Cu alloy exhibited four morphologically distinct microstructure zones which formed behind an accelerating solidification interface and have been discussed in the literature previously [38]. Sequences of nanosecond duration laser pulses with different laser pulse energies have been used to expose the morphologically different regions of the RS microstructure of the Al-10Cu alloy to additional thermal transients that resulted in non-isothermal annealing and/or partial melting. Transformation pathways of the non-equilibrium features of the distinct characteristic regions of the RS microstructure in hypoeutectic Al-10Cu alloy in response to sequences of non-isothermal heating-cooling transients imposed by additional laser irradiation annealing have been discussed.

The main results and conclusions of this study are as follows:

1. An apparent reduction of the threshold laser power required to induce partial or complete melting of the Al-10Cu was observed for sequences of thermal transients induced by multiple laser irradiation pulses. This has been attributed to changes of multi-phase RS microstructure, chiefly scale coarsening, in response to the non-isothermal transients of the initially nanocrystalline multiphase alloy microstructure. It has been proposed that the coarsened microstructural features resulted in enhanced conversion of the incident photon energy to heat by reducing the optical reflectivity, effectively reducing the laser power required to induce melting of the Al-10Cu.
2. Pulsed laser irradiation of the nanoscale features established in the multiphase RS microstructure of Al-10Cu resulted in coarsening of the microstructure, morphological changes, and phase transformations of the metastable phases, namely, supersaturated solid solution α-Al phase and nanoscale θ'-Al_2Cu phase, to form thermodynamically more stable phases (i.e., solid solution α-Al phase), scale coarsened θ'-Al_2Cu phase, and θ-Al_2Cu phase.

3. Formation of nanoscale precipitates of θ-Al_2Cu phase was facilitated by heterogeneous nucleation and subsequent growth in response to the laser pulse induced thermal transients. Heterogeneous nucleation of θ-Al_2Cu phase involved both the supersaturated α-Al and the θ'-Al_2Cu phase, resulting in different sets of orientation relationships equivalent to the Guinier I and Guinier II/III orientation relationships for θ-Al_2Cu and α-Al.
4. Exposure to subsequent thermal transients transformed the banded morphology grains with their characteristically alternating single-phase and multi-phase bands observed in the central regions of the RS microstructure of the Al-10Cu to a more homogenous morphology multiphase microstructure, and via partial melting to an equiaxial nano-crystalline structure for the α-Al phase, the primary solidification product.
5. The scale coarsening and morphological changes affected for the morphologically different characteristic regions of the RS microstructure by exposure to the additional non-isothermal and rapid transients will change mechanical and other physical properties. Improved understanding of the response of multiphase RS microstructures of multicomponent alloys to subsequent non-isothermal transient exposures may offer opportunity for the development of strategies for tailoring the local microstructure and thus the properties of SLM AM components.

Declaration of Competing Interest

The authors declare that they have no known competing financial interests or personal relationships that could have appeared to influence the work reported in this paper.

Acknowledgements

The research activities at the University of Pittsburgh received support from the National Science Foundation, Division of Materials Research, Metals & Metallic Nanostructures program through Grant No. DMR 1607922. Work at Lawrence Livermore National Laboratory (LLNL) was performed under the auspices of the U.S. Department of Energy by LLNL under Contract No. DE-AC52-07NA27344.

Data Availability

The raw/processed data required to reproduce these findings cannot be shared at this time as the data also forms part of an ongoing study.

References

[1] Y. Zhang, L. Wu, X. Guo, S. Kane, Y. Deng, Y.G. Jung, J.H. Lee, J. Zhang, Additive Manufacturing of Metallic Materials: A Review, J. Mater. Eng. Perform. 27 (2018) 1–13. doi:10.1007/s11665-017-2747-y.

[2] N. Haghdadi, M. Laleh, M. Moyle, S. Primig, Additive manufacturing of steels: a review of achievements and challenges, J. Mater. Sci. 56 (2021) 64–107. doi:10.1007/s10853-020-05109-0.

[3] T. DebRoy, H.L. Wei, J.S. Zuback, T. Mukherjee, J.W. Elmer, J.O. Milewski, A.M. Beese, A. Wilson-Heid, A. De, W. Zhang, Additive manufacturing of metallic components – Process, structure and properties, Prog. Mater. Sci. 92 (2018) 112–224. doi:10.1016/j.pmatsci.2017.10.001.

[4] S. Pauly, P. Wang, U. Kühn, K. Kosiba, Experimental determination of cooling rates in selectively laser-melted eutectic Al-33Cu, Addit. Manuf. 22 (2018) 753–757. doi:https://doi.org/10.1016/j.addma.2018.05.034.

[5] I. Gibson, D. Rosen, B. Stucker, 3D Printing, Rapid Prototyping, and Direct Digital Manufacturing, 2015. http://link.springer.com/10.1007/978-1-4939-2113-3.

[6] H.H. König, N.H. Pettersson, A. Durga, S. Van Petegem, D. Grolimund, A.C. Chuang, Q. Guo, L. Chen, C. Oikonomou, F. Zhang, G. Lindwall, Solidification modes during additive manufacturing of steel revealed by high-speed X-ray diffraction, Acta Mater. 246 (2023). doi:10.1016/j.actamat.2023.118713.

[7] S. Ghosh, Predictive modeling of solidification during laser additive manufacturing of nickel superalloys: Recent developments, future directions, Mater. Res. Express. 5 (2018). doi:10.1088/2053-1591/aaa04c.

[8] W. Kurz, D.J. Fisher, Fundamentals of solidification, Fourth Rev, Trans Tech Publications, Zurich, Switzerland, 1998.

[9] X. Wang, K. Chou, Effects of thermal cycles on the microstructure evolution of Inconel 718 during selective laser melting process, Addit. Manuf. 18 (2017) 1–14. doi:10.1016/j.addma.2017.08.016.

[10] W.J. Sames, K.A. Unocic, R.R. Dehoff, T. Lolla, S.S. Babu, Thermal effects on microstructural heterogeneity of Inconel 718 materials fabricated by electron beam melting, J. Mater. Res. 29 (2014) 1920–1930. doi:10.1557/jmr.2014.140.

[11] T. Zhang, H. Li, H. Gong, Y. Wu, X. Chen, X. Zhang, Study on location-related thermal cycles and microstructure variation of additively manufactured inconel 718, J. Mater. Res. Technol. 18 (2022) 3056–3072. doi:10.1016/j.jmrt.2022.03.178.

[12] Y. Kok, X.P. Tan, P. Wang, M.L.S. Nai, N.H. Loh, E. Liu, S.B. Tor, Anisotropy and heterogeneity of microstructure and mechanical properties in metal additive manufacturing: A critical review, Mater. Des. 139 (2018) 565–586. doi:10.1016/j.matdes.2017.11.021.

[13] D. Zheng, Z. Li, Y. Jiang, R. Li, Y. Wu, Y. Tu, X. Cheng, P. Fu, L. Peng, H. Tang, Effect of multiple thermal cycles on the microstructure evolution of GA151K alloy fabricated by laser-directed energy deposition, Addit. Manuf. 57 (2022) 102957. doi:https://doi.org/10.1016/j.addma.2022.102957.

[14] S. Cheruvathur, E.A. Lass, C.E. Campbell, Additive Manufacturing of 17-4 PH Stainless Steel: Post-processing Heat Treatment to Achieve Uniform Reproducible Microstructure, Jom. 68 (2016) 930–942. doi:10.1007/s11837-015-1754-4.

[15] R. Jiang, A. Mostafaei, Z. Wu, A. Choi, P.W. Guan, M. Chmielus, A.D. Rollett, Effect of heat treatment on microstructural evolution and hardness homogeneity in laser powder bed fusion of alloy 718, Addit. Manuf. 35 (2020) 101282. doi:10.1016/j.addma.2020.101282.

[16] F. Zhang, L.E. Levine, A.J. Allen, M.R. Stoudt, G. Lindwall, E.A. Lass, M.E. Williams, Y. Idell, C.E. Campbell, Effect of heat treatment on the microstructural evolution of a nickel-based superalloy additive-manufactured by laser powder bed fusion, Acta Mater. 152 (2018) 200–214. doi:10.1016/j.actamat.2018.03.017.

[17] S.M. Yeon, J. Yoon, T.B. Kim, S.H. Lee, T.S. Jun, Y. Son, K. Choi, Normalizing Effect of Heat Treatment Processing on 17-4 PH Stainless Steel Manufactured by Powder Bed Fusion, Metals (Basel). 12 (2022). doi:10.3390/met12050704.

[18] D. Vaughan, J.M. Silcock, Electron microsocpe observations of the formation of θ from θ′ in Al-4%Cu, Acta Metall. 12 (1964) 1463–1466.

[19] D. Vaughan, J.M. Silcock, The Orientation and Shape of Theta Precipitates Formed in an Al-Cu Alloy, Phys. Status Solidi. 20 (1967) 725–736. doi:10.1002/pssb.19670200235.

[20] J.L. Murray, The aluminium-copper system, Int. Met. Rev. 30 (1985) 211–233. doi:10.1179/imtr.1985.30.1.211.

[21] C. Laird, H.I. Aaronson, Mechanisms of formation of θ and dissolution of θ′ precipitates in an Al-4% Cu alloy, Acta Metall. 14 (1966) 171–185. doi:10.1016/0001-6160(66)90298-7.

[22] C. Liu, S.K. Malladi, Q. Xu, J. Chen, F.D. Tichelaar, X. Zhuge, H.W. Zandbergen, In-situ STEM imaging of growth and phase change of individual CuAlX precipitates in Al alloy, Sci. Rep. 7 (2017) 2184. doi:10.1038/s41598-017-02081-9.

[23] S.K. Kang, C. Laird, PRECIPITATION IN THIN FOILS OF Al- wt .% Cu ALLOY-II . GROWTH KINETICS OF 8 PRECIPITATES, Acta Metall. 23 (1975) 35–49.

[24] J.T. McKeown, K. Zweiacker, C. Liu, D.R. Coughlin, A.J. Clarke, J.K. Baldwin, J.W. Gibbs, J.D. Roehling, S.D. Imhoff, P.J. Gibbs, D. Tourret, J.M.K. Wiezorek, G.H. Campbell, Time-Resolved In Situ Measurements During Rapid Alloy Solidification: Experimental Insight for Additive Manufacturing, JOM. 68 (2016) 985–999. doi:10.1007/s11837-015-1793-x.

[25] T. LaGrange, B.W. Reed, D.J. Masiel, Movie-mode dynamic electron microscopy, MRS Bull. 40 (2015) 23–28. doi:10.1557/mrs.2014.282.

[26] G. Thomas, M.J. Whelan, Observation of precipitation in thin foils of aluminium +4% copper alloy, Philos. Mag. A J. Theor. Exp. Appl. Phys. Ser. 8. 6 (1961) 1103–1114.

[27] S. Mader, S. Herd, Formation of second phase particles in aluminum-copper alloy films, Thin Solid Films. 10 (1972) 377–389. doi:10.1016/0040-6090(72)90209-X.

[28] D.R. Frear, J.E. Sanchez, A.D. Romig, J.W. Morris, The evolution of microstructure in Al-2 Pct Cu thin films: Precipitation, dissolution, and reprecipitation, Metall. Trans. A. 21 (1990) 2449–2458. doi:10.1007/BF02646989.

[29] A. Guinier, The mechanism of precipitation in a crystal of solid metallic solution-Case of aluminum-copper and aluminum-silver systems., J. Phys. Radium. 3 (1942) 124–136. https://doi.org/10.1051/jphysrad:0194200307012400%0A.

[30] J.T. McKeown, A.K. Kulovits, C. Liu, K. Zweiacker, B.W. Reed, T. Lagrange, J.M.K. Wiezorek, G.H. Campbell, In situ transmission electron microscopy of crystal growth-mode transitions during rapid solidification of a hypoeutectic Al-Cu alloy, Acta Mater. 65 (2014) 56–68. doi:10.1016/j.actamat.2013.11.046.

[31] W. Kurz, R. Trivedi, Rapid solidification processing and microstructure formation, Mater. Sci. Eng. A. 179–180 (1994) 46–51. doi:10.1016/0921-5093(94)90162-7.

[32] R. Trivedi, W. Kurz, Dendritic growth, Int. Mater. Rev. 39 (1994) 49–74. https://doi.org/10.1179/imr.1994.39.2.49.

[33] K.W. Zweiacker, C. Liu, M.A. Gordillo, J.T. McKeown, G.H. Campbell, J.M.K. Wiezorek,

Composition and automated crystal orientation mapping of rapid solidification products in hypoeutectic Al-4 at.%Cu alloys, Acta Mater. 145 (2018) 71–83. doi:10.1016/j.actamat.2017.11.040.

[34] M. Carrard, M. Gremaud, M. Zimmermann, W. Kurz, About the banded structure in rapidly solidified dendritic and eutectic alloys, Acta Metall. Mater. 40 (1992) 983–996. doi:10.1016/0956-7151(92)90076-Q.

[35] W. Zimmermann, M; Carrard, M; Kurz, Rapid soldification of Al-Cu eutectic alloy by laser remelting, Acta Met. 37 (1989) 3305–3313.

[36] B. Vishwanadh, J. Jo, C.S. Bonifacio, J.M.K. Wiezorek, Site-specific preparation of plan-view samples with large field of view for atomic resolution STEM and TEM studies of rapidly solidified multi-phase AlCu thin films, Mater. Charact. 189 (2022) 111943. doi:https://doi-org.lakshya.remotexs.in/10.1016/j.matchar.2022.111943.

[37] Y. Liu, K. Zweiacker, C. Liu, J.T. Mckeown, J.M.K. Wiezorek, Transmission electron microscopy of the rapid solidification microstructure evolution and solidification interface velocity determination in hypereutectic Al-20at.%Cu after laser melting, Acta Mater. Under Revi (2023). http://dx.doi.org/10.2139/ssrn.4455114.

[38] B. Vishwanadh, C. Liu, K. Zweiacker, J. McKeown, J.M.K. Wiezorek, Interface velocity dependent solute trapping and phase selection during rapid solidification of laser melted hypo-eutectic Al-11at.%Cu alloy, Acta Mater. 195 (2020) 341–357. doi:10.1016/j.actamat.2020.04.006.

[39] J.D. Roehling, D.R. Coughlin, J.W. Gibbs, J.K. Baldwin, J.C.E. Mertens, G.H. Campbell, A.J. Clarke, J.T. McKeown, Rapid solidification growth mode transitions in Al-Si alloys by dynamic transmission electron microscopy, Acta Mater. 131 (2017) 22–30. doi:10.1016/j.actamat.2017.03.061.

[40] K. Ji, E. Dorari, A.J. Clarke, A. Karma, Microstructural Pattern Formation during Far-from-Equilibrium Alloy Solidification, Phys. Rev. Lett. 130 (2023) 26203. doi:10.1103/PhysRevLett.130.026203.

[41] P. Jreidini, T. Pinomaa, J.M.K. Wiezorek, J.T. McKeown, A. Laukkanen, N. Provatas, Orientation Gradients in Rapidly Solidified Pure Aluminum Thin Films: Comparison of Experiments and Phase-Field Crystal Simulations, Phys. Rev. Lett. 127 (2021) 205701. doi:10.1103/PhysRevLett.127.205701.

[42] T. Pinomaa, J.M. McKeown, J.M.K. Wiezorek, N. Provatas, A. Laukkanen, T. Suhonen, Phase field modeling of rapid resolidification of Al-Cu thin films, J. Cryst. Growth. 532 (2020) 125418. doi:https://doi.org/10.1016/j.jcrysgro.2019.125418.

[43] H. Yeung, J. Chen, G. Yang, Y. Guo, D. Lin, W. Tan, J. Weaver, Effect of spiral scan strategy on microstructure for additively manufactured stainless steel 17–4, Manuf. Lett. 29 (2021) 1–4. doi:10.1016/j.mfglet.2021.04.005.

[44] X. Chen, C. Qiu, In-situ development of a sandwich microstructure with enhanced ductility by laser reheating of a laser melted titanium alloy, Sci. Rep. 10 (2020) 1–12. doi:10.1038/s41598-020-72627-x.

[45] W. Xu, E.W. Lui, A. Pateras, M. Qian, M. Brandt, In situ tailoring microstructure in additively manufactured Ti-6Al-4V for superior mechanical performance, Acta Mater. 125 (2017) 390–400. doi:10.1016/j.actamat.2016.12.027.

[46] K. Zhou, D. Cui, Z. Chai, Y. Zhang, Z. Yang, C. Zhu, Z. Wang, J. Li, J. Wang, In-situ tailoring microstructures to promote strength-ductility synergy in laser powder bed fusion of NiCoCr medium-entropy alloy, Addit. Manuf. 66 (2023) 103443. doi:https://doi.org/10.1016/j.addma.2023.103443.

[47] C. Taudt (2022), Surface Profilometry. . In: Development and Characterization of Dispersion-Encofded Method for Low-Coherence Interferometry, pp. 39–88. doi:10.1007/978-3-658-35926-3_3.

[48] K. Zweiacker, J.T. McKeown, C. Liu, T. Lagrange, B.W. Reed, G.H. Campbell, J.M.K. Wiezorek, Determination of crystal growth rates during rapid solidification of polycrystalline aluminum by nano-scale spatio-temporal resolution in situ transmission electron microscopy, J. Appl. Phys. 120 (2016) 055106 (1–11). doi:10.1063/1.4960443.

[49] E.F. Rauch, M. Véron, Automated crystal orientation and phase mapping in TEM, Mater. Charact. 98 (2014) 1–9. doi:10.1016/j.matchar.2014.08.010.

[50] D.A. Porter, K.E. Easterling, M.Y. Sherif, Phase Transformations in Metals and Alloys, Third edit, CRC Press, Florida, USA, 1992.

[51] P.A. Stadelmann, EMS - a software package for electron diffraction analysis and HREM image simulation in materials science, Ultramicroscopy. 21 (1987) 131–145. doi:10.1016/0304-3991(87)90080-5.

[52] P. Stadelmann, Image analysis and simulation software in transmission electron

microscopy, Microsc. Microanal. 9 (2003) 60–61. doi:10.1017/s1431927603012224.